Lithosphere

Research Article

Mechanical Responses of Underground Unparallel-Fissured Rocks Subjected to Coupled Static-Dynamic Loading

Hongbo Du [1] **Haoran Wang,** [1] **Peng Feng** [2,3] **Renjie Tian,** [1] **and Yi Wang** [2]

[1]*National Inland Waterway Regulation Engineering Technology Research Center, Chongqing Jiaotong University, Chongqing 400074, China*
[2]*School of Architecture and Civil Engineering, Chengdu University, Chengdu, Sichuan 610106, China*
[3]*Sichuan Engineering Research Center for Mechanical Properties and Engineering Technology of Unsaturated Soils, Chengdu University, Chengdu, Sichuan 610106, China*

Correspondence should be addressed to Peng Feng; fengpengfx@163.com

Preexisting fissures within a natural rock mass significantly affect the mechanical responses of underground engineering rocks when subjected to coupled static-dynamic loads. Understanding the dynamic mechanical responses of prestressed fissured rocks is beneficial for optimizing the stability of rock engineering structures. Based on the split Hopkinson pressure bar (SHPB) device, a series of coupled static-dynamic compression tests were systematically performed to investigate the mechanical properties, the failure behaviors, the fragment characteristics, and the energy dissipation of unparallel-fissured rocks. Results show that the coupled dynamic strength increases with the applied strain rate for a given static prestress, while the elastic modulus does not exhibit any clear loading rate dependence. Under the given strain rate, the fissured sandstone has the highest strength under the static prestress of 0.6 uniaxial compressive strength (σ_s), followed by the static prestress of 0.4 σ_s, 0.2 σ_s, and 0.8 σ_s. The failure modes of fissured sandstone highly depend on the dynamic strain rate, and the ultimate failure pattern gradually changes from the mixed tensile-shear failure mode to the shear failure dominant mode with increasing strain rate. With an increasing dynamic strain rate, fissured rocks should absorb more energy in a short time, which results in more crack formation in the failure process. A higher static prestress can induce greater energy dissipation density and energy utilization efficiency when the static prestress is less than 0.8 σ_s. In addition, the relationships between energy dissipation and mechanical response of fissured sandstones under coupled static-dynamic loads are established and discussed.

1. Introduction

Engineering rock structures can be considered complex geological media, which generally contain many discontinuities involving joints, fissures, weak surfaces, and faults [1, 2]. In practice, the underground fissured rocks are likely subjected to not only the in situ stress from the gravity stress and tectonic stress [3–5], but the exterior dynamic disturbances induced by engineering blasting or drilling [6–10], both of which result in a coupled static-dynamic loading [11–13], as shown in Figure 1. Thus, understanding the mechanical behaviors of rock materials with unparallel fissures under both precompression and dynamic loads is of great signifi-

cance for the rational design of underground rock engineering structures [14, 15].

To date, many studies have been conducted to reveal the mechanical behaviors and failure mechanism of fissured rocks [16–18] or rock-like materials [19, 20]. The mechanical behaviors of rock or rock-like materials can be significantly influenced by the fissure configuration, including the fissure inclination angle [21–23], fissure length [24], fissure arrangement [25], spacing [26], and rock bridging angle [27, 28]. These studies found that the preexisting fissures can evidently weaken the strength and deformation properties of specimens, and the weak degree highly depends on the fissure configuration. Specimens with different fissure
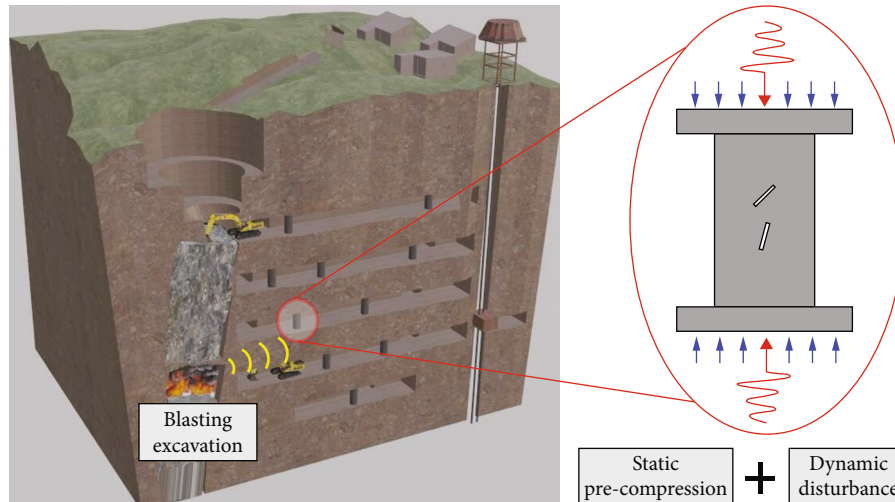
FIGURE 1: Field rock masses with unparallel fissures subjected to coupled static-dynamic disturbance.

geometries induce different cracking paths and failure modes. In general, three types of cracks appear in the fissured specimen during the loading process: tensile wing cracks, shear cracks, and mixed tensile-shear cracks [27]. The local tensile strain concentration below or above the fissure tip leads to wing or antiwing cracks, while the local compressive strain concentration near the fissure tip is related to shear cracks. Moreover, several crack coalescence modes of fissured specimens have been summarized based on the three basic crack types: tensile cracks (wing cracks), shear cracks, and mixed tensile and shear cracks [27, 29, 30].

The mechanical properties and failure mechanisms of fissured rocks or rock-like materials under dynamic loads are more complicated compared with these under static loads, [31]. The static loading test mainly studies the physical properties and fracture mechanism of rock specimens, while the relationship between strain rate, mechanical parameters, and energy dissipation has become the focus of dynamic research. Zou et al. [32, 33] and Li et al. [34, 35] investigated the effect of the dynamic strain rate and fissure inclination angle on the mechanical properties and failure mechanism of rock materials with single and double fissures using the split Hopkinson pressure bar (SHPB) equipment. Traditional mechanical parameters (strength and elastic modulus) of fissured rocks show evident loading-rate dependence. Unlike fissured rocks under static loading, the shear cracks mainly control the failure patterns of fissured rocks under dynamic loads, featuring X or half-X shear belts at the end of loading. Yan et al. [36] further studied the mechanical behaviors of fissured sandstone with multiple fissures subjected to dynamic loading conditions and found similar weakening results, i.e., the mechanical parameters of fissured rocks decrease with increasing fissure intensity for a given dynamic strain rate. However, the energy dissipation densities cannot be significantly influenced via the fissure intensity. Several crack coalescence modes of fissured specimens have been summarized based on three basic crack types: tensile cracks (wing cracks), shear cracks, and mixed tensile and shear cracks [29, 30].

Existing attempts on rock specimens were mainly concentrated on the preexisting fissures with parallel configurations. In fact, fissures in field rock masses generally appear in an unparallel arrangement. Compared with the specimens containing parallel fissures, the crack coalescence behaviors and stress distribution of the specimens containing unparallel fissures are more complex [37]. To date, few scholars have studied the effects of unparallel fissures on the mechanical properties of rock specimens, and the mechanical parameters and crack coalescence modes were mainly investigated. Lee and Jeon [38, 39] studied the cracking behavior of brittle materials with two unparallel fissures composed of a horizontal fissure and an underlying inclined fissure of 30-90°. Yang et al. [40] investigated the effects of inclination angle on the mechanical behaviors of red sandstone with two unparallel fissures, where the inclination angle of the upper fissure was fixed at 45°. Huang et al. [41] experimentally and numerically revealed the macro- and micromechanism of rock specimens with unparallel fissures and identified four crack types. Feng et al. [14] used an MTS rock testing apparatus to investigate the mechanical behaviors and energy dissipation characteristics of rock-like materials subjected to coupled static-dynamic loading with the strain rates of 10^{-4}-10^{-2} s^{-1}.

So far, existing research on specimens containing unparallel fissures is rare, especially under coupled static and dynamic loading conditions, which result in a limited understanding of the mechanical behaviors of underground unparallel-fissured rock materials subjected to dynamic disturbance. This study intends to explore the effect of the coupled static-dynamic strain rate on the mechanical behaviors of unparallel-fissured rocks based on the SHPB loading system. A digital image correlation (DIC) technique is adopted to analyze the fracture mechanism of unparallel-fissured rocks.

2. Materials and Methods

2.1. Specimen Preparation. A typical sandstone obtained from Neijiang, Sichuan Province of China, is utilized herein
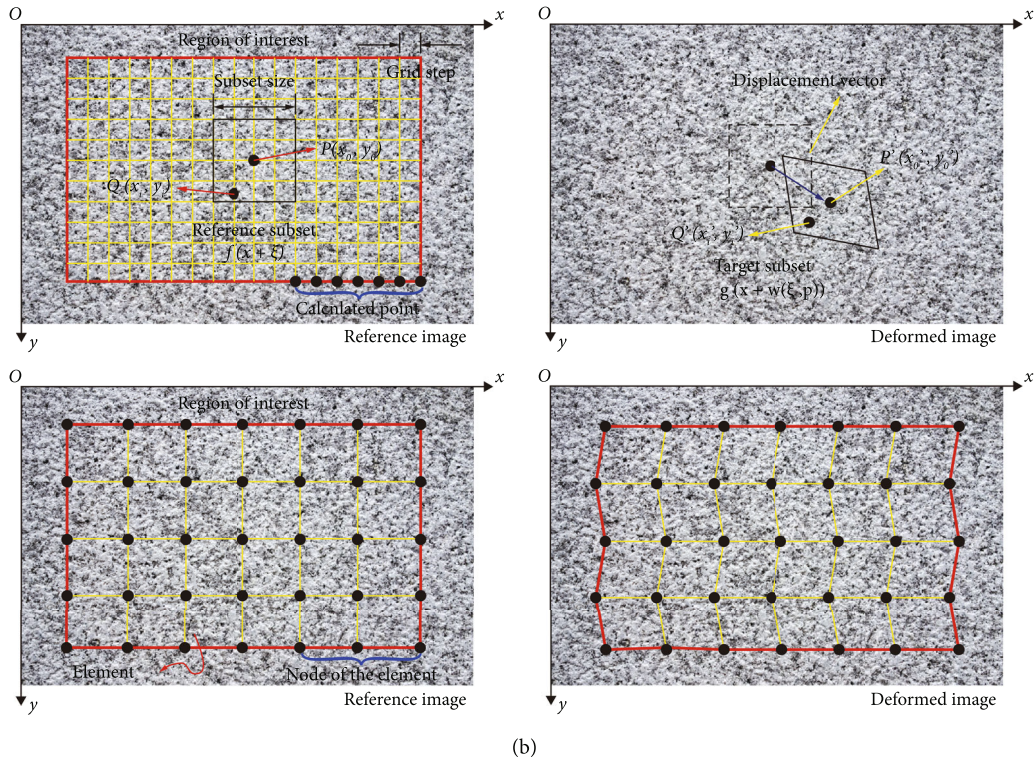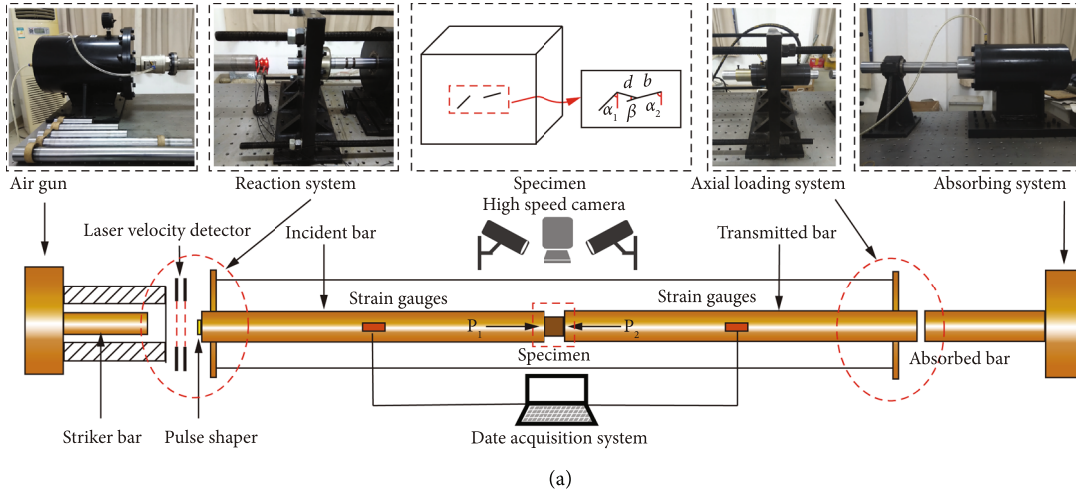
FIGURE 2: (a) Schematic diagram of the SHPB dynamic loading system and (b) the principle of DIC algorithm.

to fabricate the fissured specimens to study the mechanical properties and failure mechanism of rocks. All rock specimens are cut from the same rectangular sandstone block to systematically reduce the experimental error. Then, the specimens are cut according to the prefabricated fissure configurations. Finally, all specimens are polished, and the surface roughness is guaranteed to be less than 0.02 mm. "Fissure" is used to describe prefabricated fissures, and "crack" is used to describe the new cracks generated during the loading process. The geometric dimensions (width × thickness × height) of all rock specimens are $35 \times 35 \times 45$ mm. The detailed geometries of fissured rock specimens can be described by five parameters: fissure inclination I ($\alpha_1 = 45°$), fissure

TABLE 1: Mechanical and dimensional information of the split Hopkinson pressure bars.

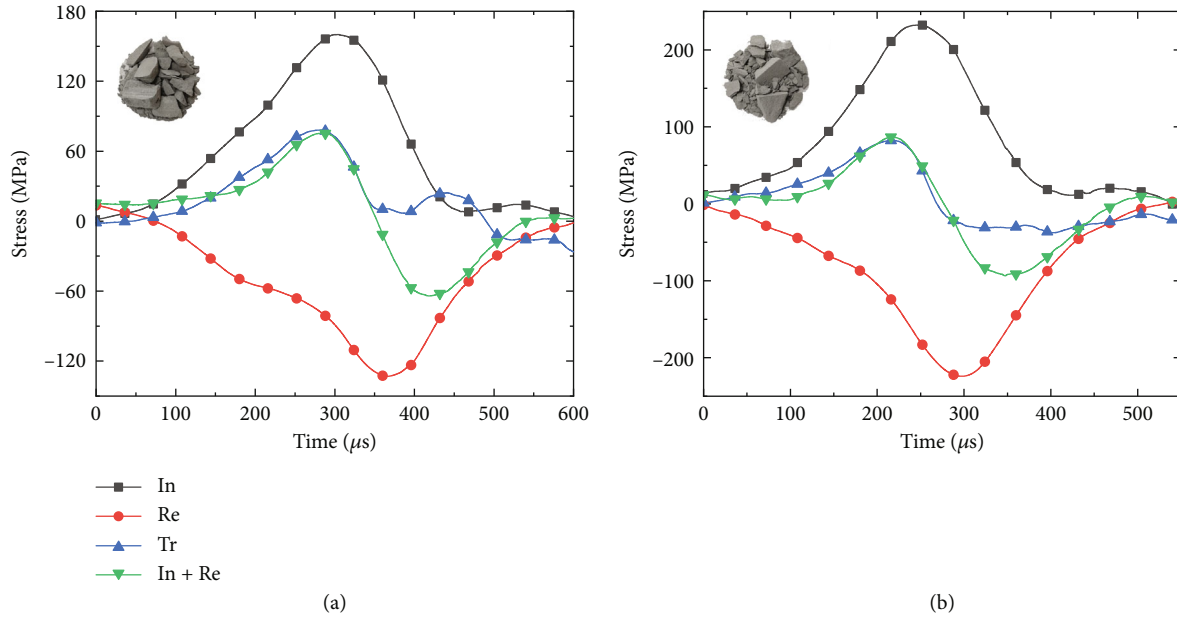| Physical parameters	Value
Diameter of the bars	50 mm
Elastic modulus of the bars	211 GPa
Density of the bars	7800 kg·m^{-3}
Length of the incident bar	3000 mm
Length of the transmit bar	2000 mm
Length of the striker bar	300 mm
Velocity of P-wave	5201 m/s

FIGURE 3: Examination of the dynamic stress equilibrium for the typical unparallel-fissured specimens: (a) No. S0.2&D2 and (b) No. S0.6&D3.

inclination II ($\alpha_2 = 75°$), fissure length ($b = 7$ mm), rock bridge length ($d = 5$ mm), and rock bridging length ($\beta = 30°$). The static uniaxial compressive strength (σ_s) and elastic modulus of the unparallel-fissured sandstone are 51.2 MPa and 5.18 GPa, respectively. In this study, all fissured specimens can be divided into four groups according to the static prestress: 0.2 σ_s, 0.4 σ_s, 0.6 σ_s, and 0.8 σ_s, which represent the typical tectonic stresses in underground rock engineering at different depths. Each fissured rock can be represented via S&DN to exhibit its suffered coupled static-dynamic loads, where S is the ratio of static prestress to uniaxial compressive strength, and DN is the ranked number of dynamic strain rate, which varies from 1 to 6. For example, S0.2&D1 is the nonparallel-fissured sandstone subjected to a static prestress of 0.2 σ_s, and the dynamic strain rate is ranked No. 1.

2.2. Testing Equipment.
As suggested by the International Society for Rock Mechanics and Rock Engineering, the SHPB is widely employed to investigate the mechanical responses of brittle materials [42–44]. SHPB consists of a striker bar, an incident bar, a transmitted bar, axial confining pressure system, and a data acquisition system, as shown in Figure 2(a). Mechanical and dimensional information of the SHPB employed in this study are listed in Table 1. The specimen is sandwiched between the incident and transmission bars, and it is initially pressured to the pre-stress in the axial direction by driving the transmitted bar moving leftwards via the axial confining pressure system. A copper sheet is utilized here to transform the rectangle stress wave into an approximately semisinusoidal shape, which facilitates the stress equilibrium between two ends of the rock specimen. Vaseline is glued on the two ends of the specimen to minimize the friction effect.

In addition, a specialized high-speed camera is used to capture the crack propagation process of the rock specimens during loading. This high-speed camera can take a series of pictures with a resolution of 256×256 pixels and a maximal shooting speed of 180000 frames per second (fps). An organic glass is established to separate the camera and rock specimen to avoid the damage of the splashing fragments to the camera. In addition, a digital image correlation (DIC) technique is employed to analyze the strain field of fissured rocks based on the captured pictures.

2.3. Data Processing.
Based on the recorded strain signals from gauges and data acquisition devices, the average dynamic stress $\sigma(t)$, strain $\varepsilon(t)$, and strain rate $\dot{\varepsilon}(t)$ can be indirectly calculated as follows [45]:

$$\dot{\varepsilon}(t) = \frac{C_{\text{bar}}}{L_{sp}} [\varepsilon_i - \varepsilon_r - \varepsilon_{tr}],$$

$$\varepsilon(t) = \int_0^t \dot{\varepsilon}(t) dt = \frac{C_{\text{bar}}}{L_{sp}} \int_0^t [\varepsilon_i - \varepsilon_r - \varepsilon_{tr}] dt, \quad (1)$$

$$\sigma(t) = \frac{A_{\text{bar}} E_{\text{bar}}}{2 A_{sp}} [\varepsilon_i + \varepsilon_r + \varepsilon_{tr}],$$

where C_{bar}, E_{bar}, and A_{bar} are the P-wave velocity, elastic modulus, and cross-sectional area of the pressure bars, respectively; L_{sp} is the length of the fissured rock specimen; and A_{sp} is the cross-sectional area of the specimen.

The dynamic loading process of the rock specimen accompanies the energy evolution. The incident energy (W_i), reflected energy (W_r), transmitted energy (W_t), and
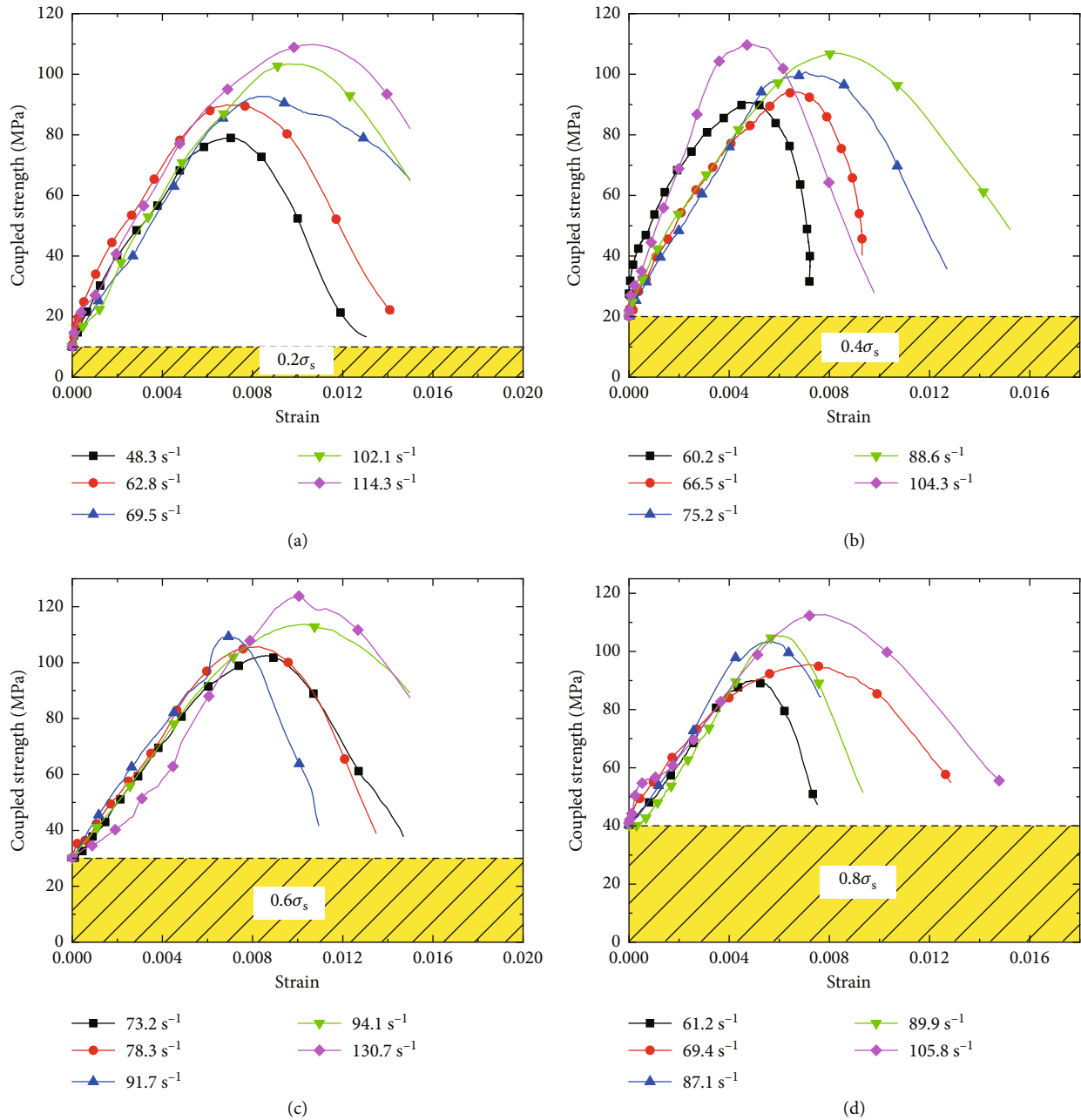
FIGURE 4: Stress-strain curves of the unparallel-fissured specimens with (a) 0.2 σ_s, (b) 0.4 σ_s, (c) 0.6 σ_s, and (d) 0.8 σ_s static prestress under different dynamic loading rates.

dissipated energy (W_d) of the fissured specimen in SHPB tests can be calculated as follows:

$$W_i = \int_0^t E_{bar} A_{bar} C_{bar} \varepsilon_i^2 dt,$$

$$W_r = \int_0^t E_{bar} A_{bar} C_{bar} \varepsilon_r^2 dt,$$

$$W_t = \int_0^t E_{bar} A_{bar} C_{bar} \varepsilon_t^2 dt,$$

$$W_d = Wi - Wr - Wt = \int_0^t E_{bar} A_{bar} C_{bar} \left(\varepsilon_i^2 - \varepsilon_r^2 - \varepsilon_t^2 \right) dt.$$

$$(2)$$

To investigate the energy dissipation and energy utilization characteristics of fissured rocks under dynamic loading conditions, the energy dissipation density D and energy utilization efficiency N of specimens are proposed, which can be determined as follows:

$$N = \frac{W_d}{W_i} = \frac{\int_0^t E_{bar} \left(\varepsilon_i^2 - \varepsilon_r^2 - \varepsilon_t^2 \right) A_{bar} C_{bar} dt}{\int_0^t E_{bar} A_{bar} C_{bar} \varepsilon_i^2 dt},$$

$$D = \frac{W_d}{V} = \int_0^t E_{bar} \left(\varepsilon_i^2 - \varepsilon_r^2 - \varepsilon_t^2 \right) A_{bar} C_{bar} \frac{dt}{V},$$

$$(3)$$

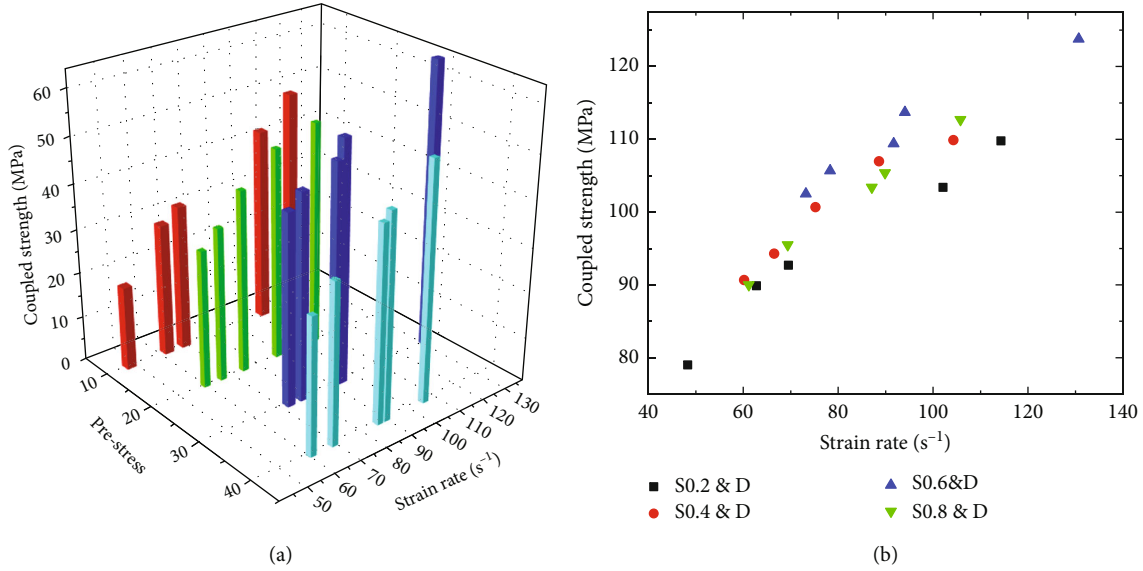where V is the volume of the rock specimen.

(a)

(b)

FIGURE 5: Coupled dynamic strength of the fissured specimens subjected to various coupled static-dynamic loads.

TABLE 2: The dynamic strength and corresponding CDIF of the unparallel-fissured specimens.

Notation	Static prestress (MPa)	Strain rate (s^{-1})	Coupled strength (MPa)	CDIF
S0.2&D1	10.1	48.3	79.0	1.54
S0.2&D2	10.1	62.8	89.9	1.76
S0.2&D3	10.1	69.5	92.7	1.81
S0.2&D4	10.1	102.1	103.4	2.02
S0.2&D5	10.1	114.3	109.8	2.14
S0.4&D1	20.1	60.2	90.7	1.77
S0.4&D2	20.1	66.5	94.3	1.84
S0.4&D3	20.1	75.2	100.7	1.97
S0.4&D4	20.1	88.6	107.0	2.09
S0.4&D5	20.1	104.3	109.9	2.15
S0.6&D1	30.2	73.2	102.5	2.00
S0.6&D2	30.2	78.3	105.7	2.06
S0.6&D3	30.2	91.7	109.4	2.14
S0.6&D4	30.2	94.1	113.7	2.22
S0.6&D5	30.2	130.7	123.8	2.42
S0.8&D1	40.3	61.2	90.0	1.76
S0.8&D2	40.3	69.4	95.5	1.87
S0.8&D3	40.3	87.1	103.4	2.02
S0.8&D4	40.3	89.9	105.4	2.06
S0.8&D5	40.3	105.8	112.7	2.20

(a)

T: Tensile wing crack
S: Shear crack
T-S: Mixed tensile-shear crack
A: Anti-wing crack
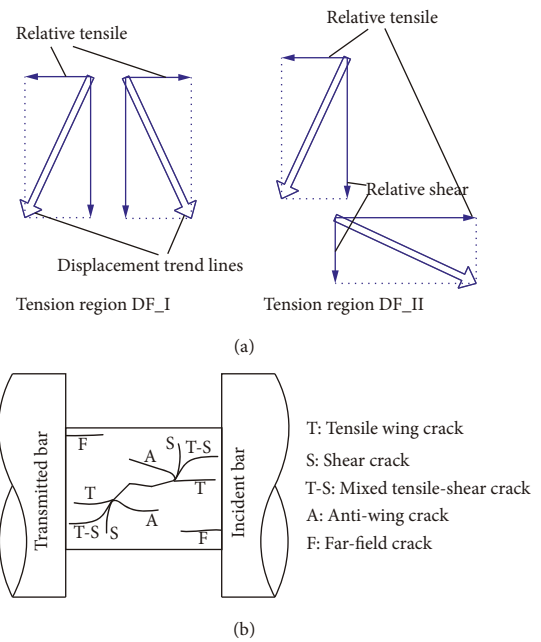F: Far-field crack

(b)

FIGURE 6: (a) Two displacement field types associated with different microcracking processes (produced after Yan et al. [54]); (b) crack types observed in this investigation (reproduced after Cheng et al. [26]).

2.4. Digital Image Correlation Technique. In this study, the open DIC software *Ncorr* is employed to investigate the evolution of strain field on the surfaces of fissured rocks [2, 46, 47]. During the 2D DIC computational process, the in-plane displacement vector is first discerned in the deformed state for each measuring point, and the entirety of the in-plane displacements can be given by the corresponding second-order displacement tensor *u*, as shown in Figure 2(b). The second-order strain tensor ε is acquired by the following equation:

$$\varepsilon = \begin{pmatrix} \varepsilon_{11} & \varepsilon_{12} \\ \varepsilon_{21} & \varepsilon_{22} \end{pmatrix} = \begin{pmatrix} \varepsilon_{xx} & \varepsilon_{xy} \\ \varepsilon_{yx} & \varepsilon_{yy} \end{pmatrix} = \begin{pmatrix} \dfrac{\partial u_x}{\partial x} & \dfrac{\partial u_x + \partial u_y}{\partial x} \\ \dfrac{\partial u_x + \partial u_y}{\partial y} & \dfrac{\partial u_y}{\partial y} \end{pmatrix},$$
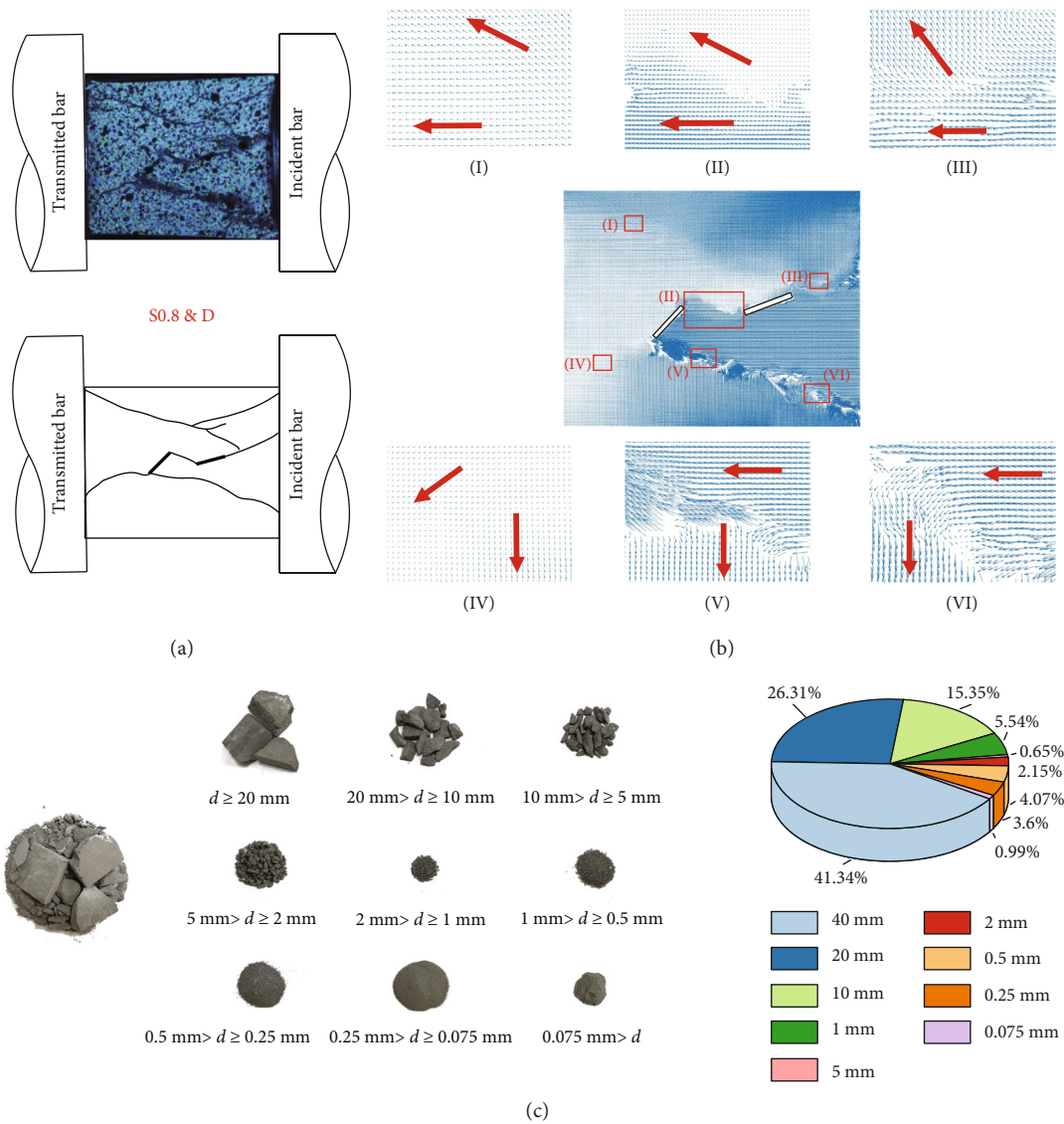
(4)

FIGURE 7: Typically mixed tensile-shear failure modes of the unparallel-fissured specimens under coupled static-dynamic loads: (a) binary image; (b) displacement vector; (c) fragment size distribution.

where u_x and u_y are the displacement tensors in the direction of the x- and y-axes, respectively. ε_{xx} and ε_{yy} are the normal strains perpendicular to the rock surface in the x- and y-direction, respectively. ε_{xy} is the shear strain parallel to the rock surface, which yields a deformation in the shape of the surface element, characterized by the shear angle $\gamma_{xy} = (\partial u_y/\partial x) + (\partial u_x/\partial y)$. For small deformation of the rock surface, the strain tensor ε can be described as follows [48]:

$$\varepsilon = \begin{pmatrix} \varepsilon_{11} & \varepsilon_{12} \\ \varepsilon_{21} & \varepsilon_{22} \end{pmatrix} = \begin{pmatrix} \varepsilon_{xx} & \varepsilon_{xy} \\ \varepsilon_{yx} & \varepsilon_{yy} \end{pmatrix} = \begin{pmatrix} \varepsilon_{xx} & \dfrac{1}{2}\gamma_{xy} \\ \dfrac{1}{2}\gamma_{yx} & \varepsilon_{yy} \end{pmatrix},$$

(5)

whereas $\varepsilon_{xy} = (1/2)\gamma_{xy}$ can only be validly adopted in the small deformation. In addition, the rotation of the measuring points cannot be accurately expressed via the displacement tensor u. Thus, rotation tensor R is proposed to represent the rotation information of the points. Considering the rotation tensor, the complete transformation tensor F can be further described as $F = R°u$. In this complete transformation system, apart from the global coordinate system x-y, two local coordinate systems are proposed: the coordinate system x'-y' expressing the undeformed points and the coordinate system x''-y'' corresponding to the deformed points. Thus, the x''- and y''- directions show the directions of ε_{xx} and ε_{yy}, respectively [49]. The principal axis transformation of the associated displacement tensor u can be conducted to acquire the independent strain values. In this 2D DIC software, all strain values can be calculated and presented for the
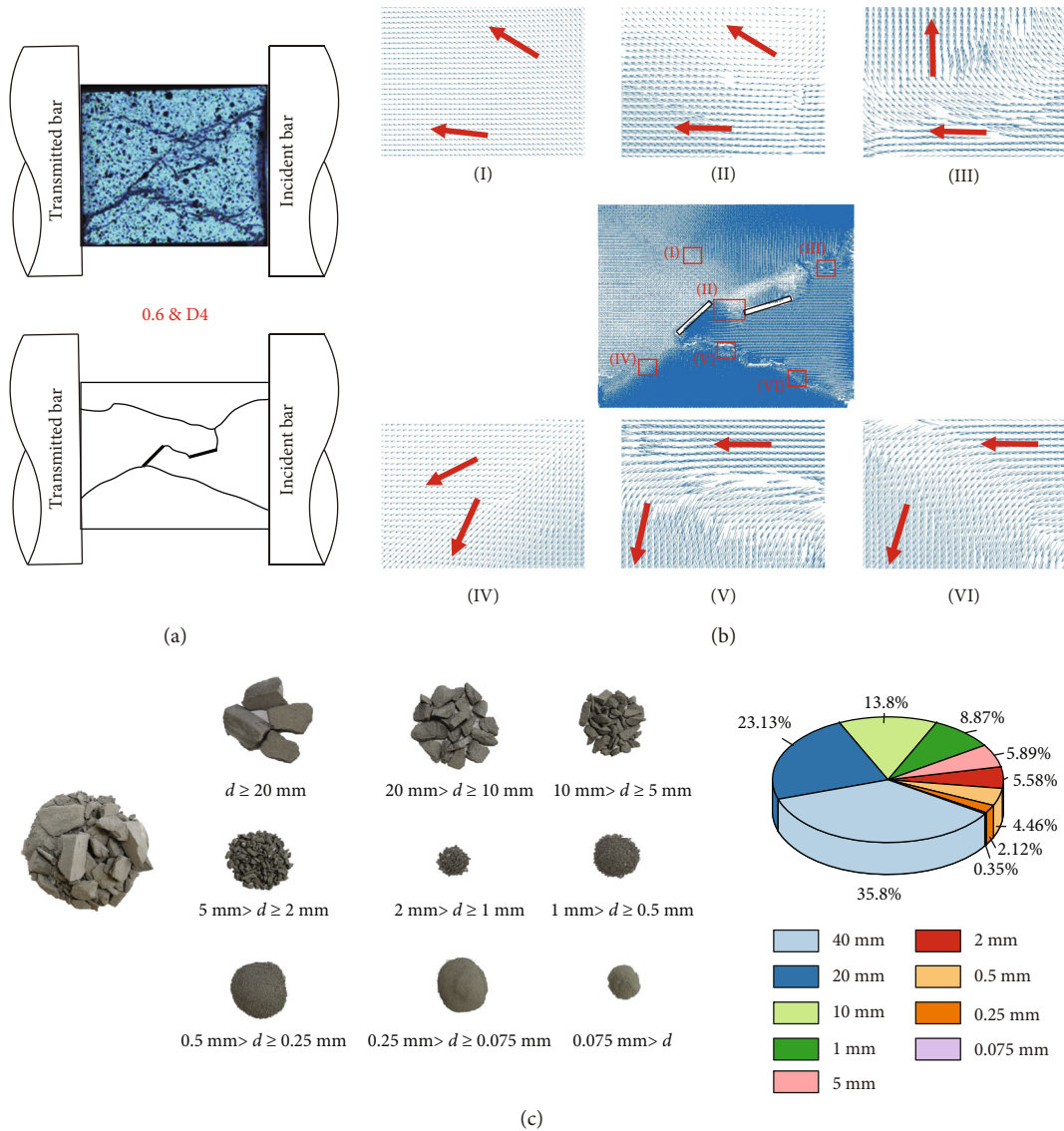
FIGURE 8: Typically shear failure modes of the unparallel-fissured specimens under coupled static-dynamic loads: (a) binary image; (b) displacement vector; (c) fragment size distribution; (d) recovered fragments.

region of interest (ROI) with different colors, and corresponding displacement and rotation vectors are shown in trajectory plots.

3. Results and Discussion

3.1. Mechanical Responses. Before processing the recorded experimental data, it is essential to verify the dynamic stress equilibrium during the loading process to guarantee the validity of the SHPB tests. Figure 3 depicts the evolution of stress-time curves in the incident and transmitted bars of the two typical unparallel-fissured specimens. Stresses in the transmitted end agree well with the sum of the incident stress and reflected stress near the peak, which demonstrates that the stress equilibrium of the unparallel-fissured specimen is achieved.

Figure 4 presents the dynamic stress–strain curves of fissured sandstone under different static prestresses of (a) 0.2 σ_s, (b) 0.4 σ_s, (c) 0.6 σ_s, and (d) 0.8 σ_s. The stress-strain curves of the rock specimens present a slow increase at the initial loading stage due to the preexisting microstructures [50]. Subsequently, the stress–strain curves sharply increase in the linear elastic stage to the peak value. After the peak stress, the stress–strain curves present a decreasing postfailure part. The stress–strain curves of fissured specimens show curve shapes after the peak stress, which may be induced via the rapid deformation of the fissured sandstone under dynamic impact.

The coupled static-dynamic strength of all fissured sandstones is shown in Figure 5 from the two-dimensional and three-dimensional perspectives, and the details are presented in Table 2. In this study, the coupled strength acquired from the sum of the prestatic stress and dynamic strength reflects
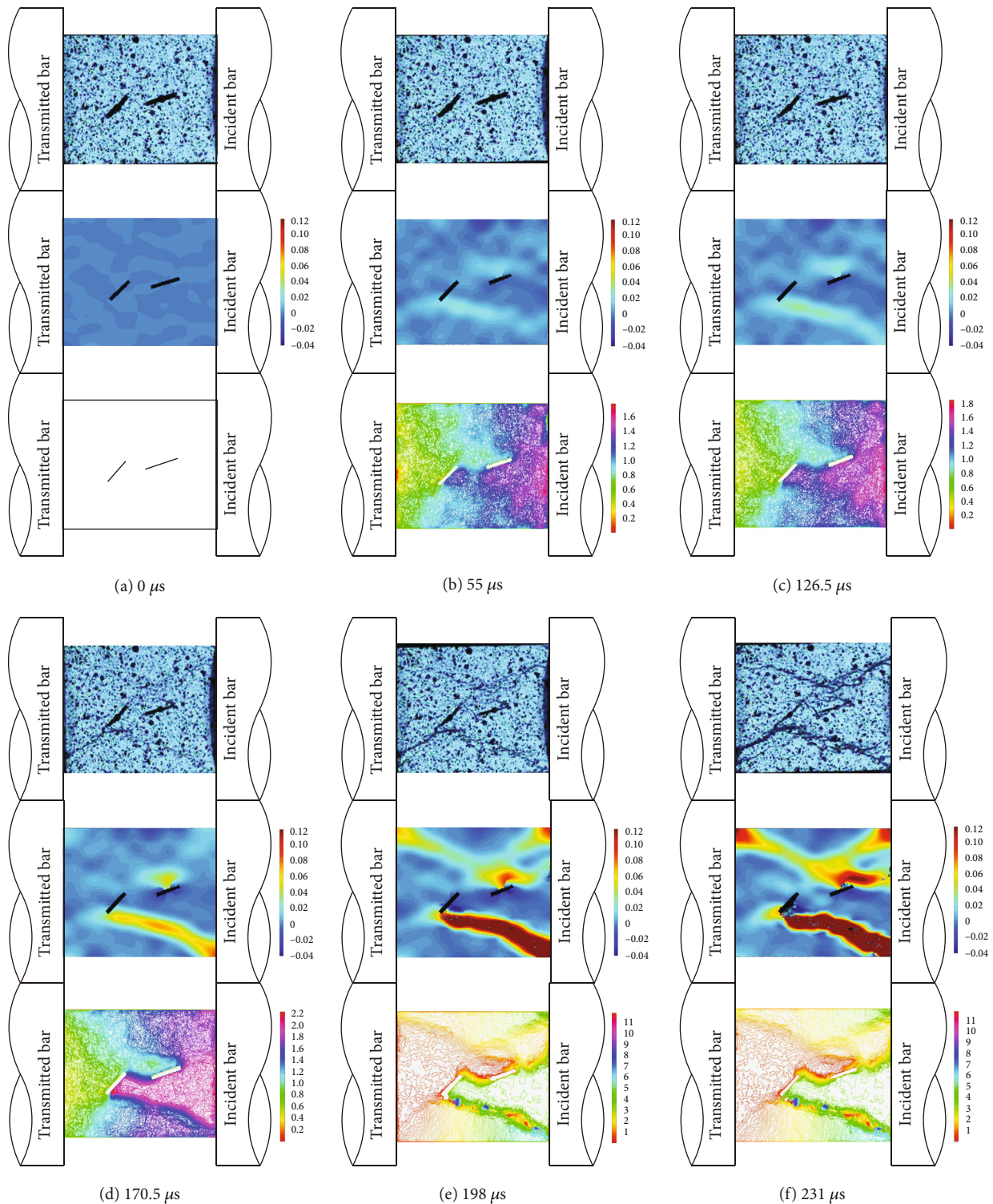
FIGURE 9: Progressive failure process of the unparallel-fissured specimen (No. S0.8&D4) with tensile-shear failure subjected to dynamic load involving laboratory image, stress field, and displacement field.

the actual bearing capacity of the fissured specimens [51]. For a given static prestress, the coupled strength of fissured rocks shows obvious loading-rate dependence. The corresponding coupled dynamic strength increase factor (CDSIF) of fissured specimens varies from 1.54 to 2.42. The axial preloading masks the fissured sandstone showed damage state before applying dynamic impacting; then, the new cracks are generated and extended within the rock material. The specimen deformation gradually decreases with increasing strain rate, and thus, the associated mechanical dynamic strength has a higher value. For a given dynamic strain rate, the coupled strength of the fissured specimen
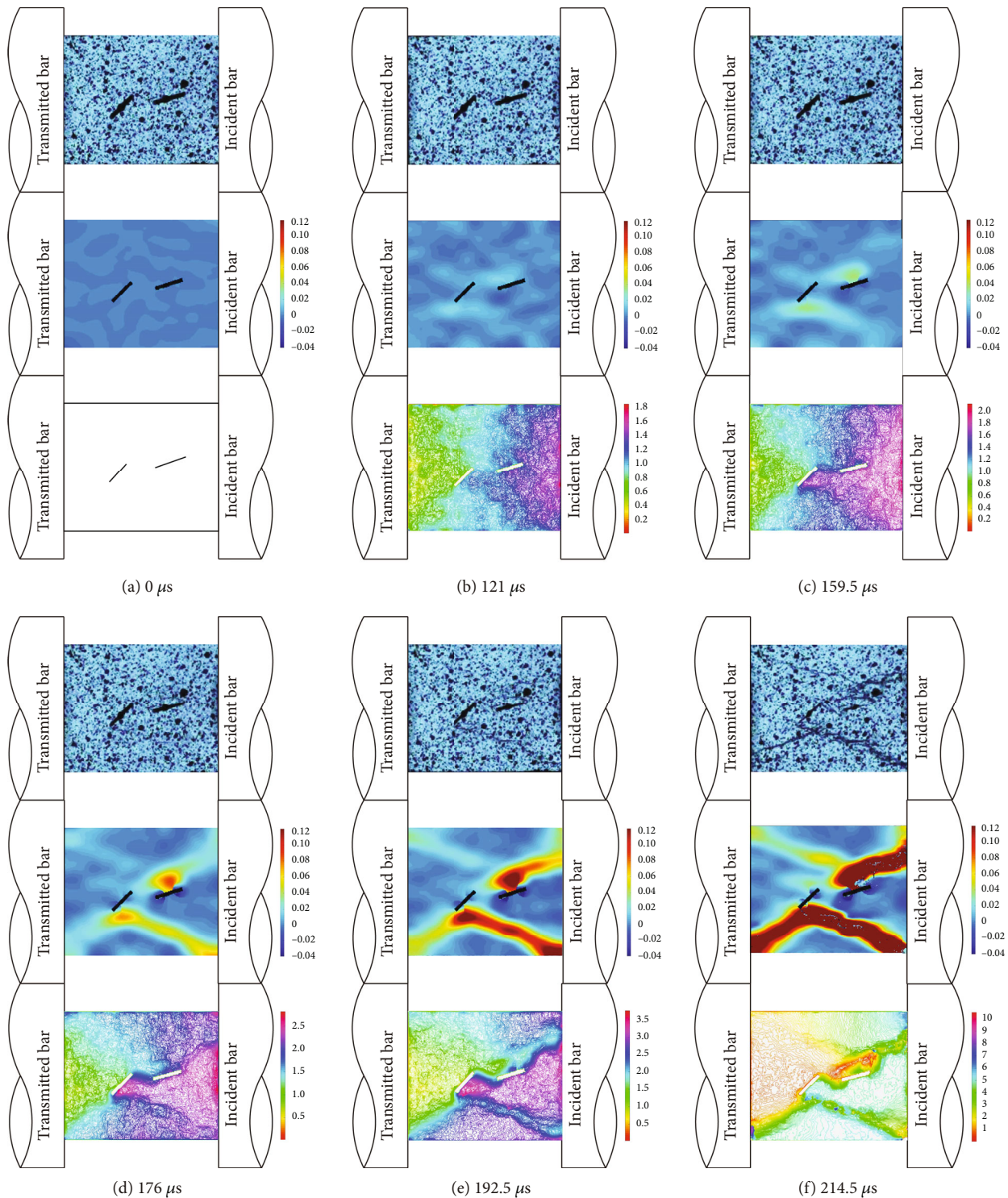
FIGURE 10: Progressive failure process of the unparallel-fissured specimen (No. S0.8&D6) with shear failure subjected to dynamic load involving laboratory image, stress field, and displacement field.

with a static prestress of 0.2 and 0.8 σ_s are lower than those of the fissured specimens under a static prestress of 0.4 σ_s, and the highest strength occurs under a static prestress of 0.6 σ_s. This result might be induced by the compressive effect on the preexisting microstructures within rock material [8, 11, 52, 53]. The dynamic responses of fissured sandstones with different prestatic loads might give some

implications for disaster prevention of the underground rock engineering projects. The coupled strength of fissured rock specimen under the static prestress of 0.6 σ_s is larger than these under other static loads, which indicates that the rock structures (e.g., rock pillars) under such in situ stress state own a higher bearing capacity, when suffer from the artificial dynamic disturbance. In addition, when the
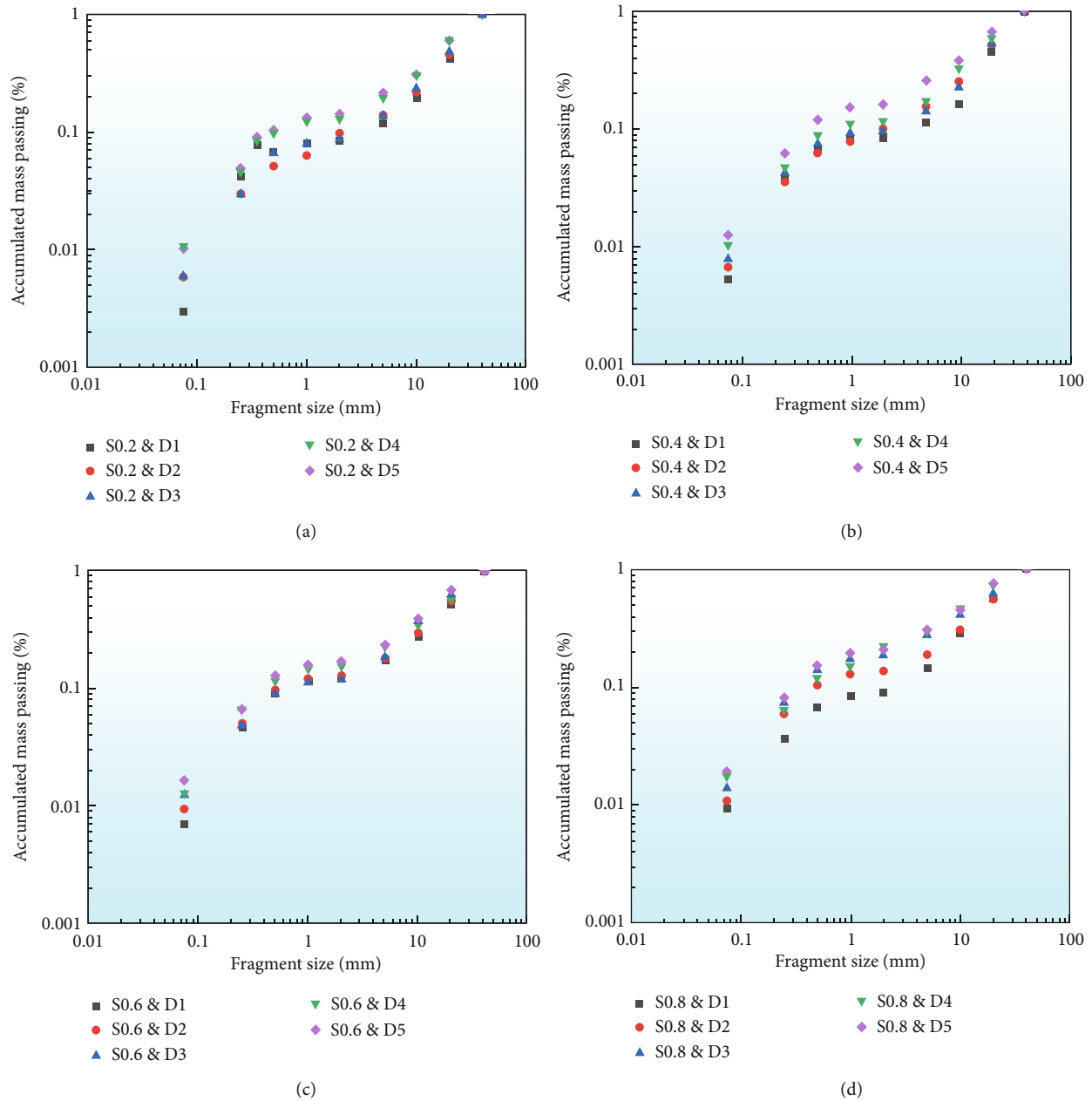
FIGURE 11: Fragment size distribution of the unparallel-fissured specimens with static prestress of (a) 0.2 σ_s, (b) 0.4 σ_s, (c) 0.6 σ_s, and (d) 0.8 σ_s under different dynamic loading rates.

burial depth of underground projects exceeds this threshold value, i.e., the static prestress of the underground rocks larger than 0.8 σ_s, the fissured rocks in the deep underground are more sensitive to the dynamic disturbance due to more microscopic cracks within the rocks induced by the in situ stress. Therefore, special attention should be paid to the mechanical responses of the static prestressed rocks under dynamic disturbance for a better design and construction of underground rock engineering projects.

3.2. Progressive Failure Behaviors. For brittle materials with preexisting fissures, new cracks generally initiate from the two tips and propagate to the upper and bottom boundaries of the fissured specimens, which results in various failure modes with the coalescence of multiple cracks. The DIC technique is employed to reveal the fracture mechanism of fissured specimens, which involves crack initiation and propagation. The full-field strain evolution and displacement field of the fissured sandstone are quantitatively analyzed and proposed two types of displacement fields to distinguish tensile cracks and shear cracks: type I (DF_I) and type II (DF_II), as shown in Figure 6(a). For type I (DF_I), the relative tensile displacement dominantly occurs in the region of the two displacement trend lines. For type II (DF_II), both displacement trend lines exhibit a relative tensile displacement and a shear displacement.
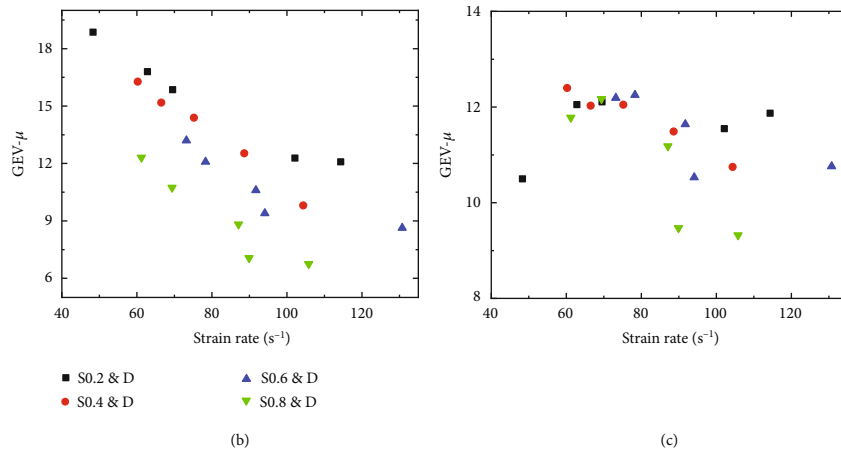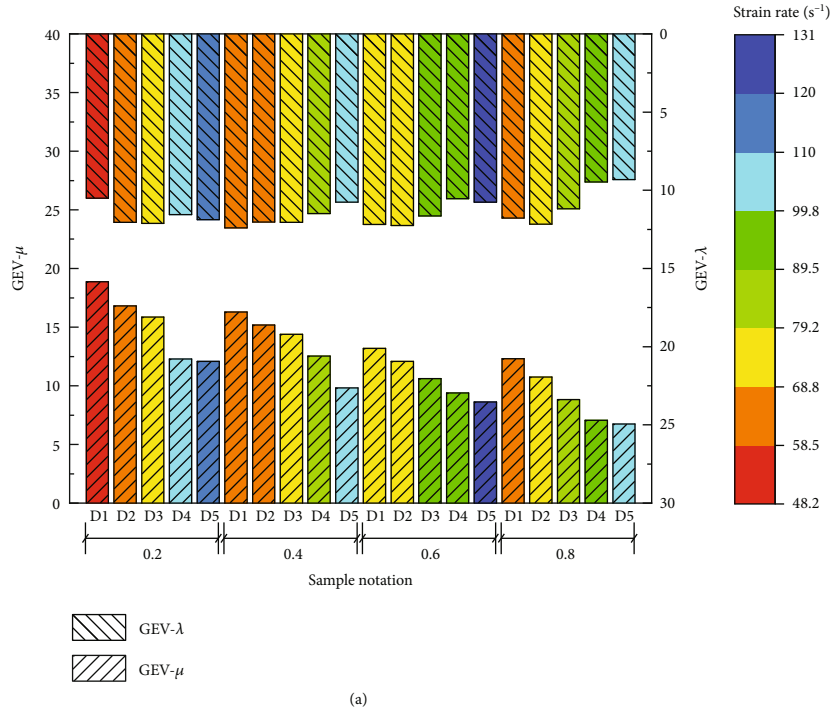
FIGURE 12: The location parameter μ and the scale parameter λ of the fragment size distribution of the unparallel-fissured specimens with GEV fitting under coupled static-dynamic loads.

As shown in Figure 6(b), five crack types are concluded based on the observation in this investigation: tensile wing cracks, shear cracks, mixed tensile-shear cracks, antiwing cracks, and far-field cracks [30, 54]. The tensile wing crack initiates from the tip of the preexisting fissure and propagates approximately along the principal stress direction, and then the crack propagates along the axial stress direction and finally extends to the two ends of the specimen. The antiwing crack initiates from the fissure tips, but the crack propagation direction is opposite to that of the tensile wing crack. Shear cracks initiate coplanar with the preexisting fissure, and their coalescence paths are parallel to the direction of the preexisting fissure. The mixed tensile-shear crack forms under the coupled effects of faradic stress and shear stress.

In this manuscript, Figures 7 and 8 show the mixed tensile-shear failure mode and shear failure mode of fissured specimens, respectively. The failure modes of fissured sandstone highly depend on the dynamic strain rate instead of static prestress.

Figure 9 depicts the evolution of the typical mixed tensile-shear failure mode of fissured sandstones subjected to coupled static-dynamic loads, which involves crack initiation, propagation, coalescence, and ultimate failure. F1 and F2 represent the preexisting fissures with inclination angle of 45 and 75, respectively. There is no obvious macroscopic crack on the surface of S0.8&D4 until the loading time reaches 50 μs, and two tensile wing cracks initiate from the two inner tips of the preexisting fissure and coalesce with each other in the bridging area. Then, a shear crack and

TABLE 3: GEV of rock specimens under different coupled static-dynamic loads.

Notation	Static prestress (MPa)	Strain rate (s⁻¹)	GEV			Average fragment size (mm)
			ζ	μ	λ	
S0.2&D1	10.1	48.3	-0.50	18.86	10.50	14.24
S0.2&D2	10.1	62.8	-0.47	16.80	12.05	13.72
S0.2&D3	10.1	69.5	-0.43	15.86	12.11	13.39
S0.2&D4	10.1	102.1	-0.29	12.28	11.55	11.60
S0.2&D5	10.1	114.3	-0.29	12.09	11.87	11.51
S0.4&D1	20.1	60.2	-0.46	16.28	12.40	14.21
S0.4&D2	20.1	66.5	-0.41	15.19	12.03	13.04
S0.4&D3	20.1	75.2	-0.38	14.40	12.05	13.01
S0.4&D4	20.1	88.6	-0.27	12.54	11.49	11.81
S0.4&D5	20.1	104.3	-0.13	9.81	10.75	10.46
S0.6&D1	30.2	73.2	-0.35	13.20	12.19	12.09
S0.6&D2	30.2	78.3	-0.27	12.09	12.25	11.07
S0.6&D3	30.2	91.7	-0.20	10.60	11.64	10.72
S0.6&D4	30.2	94.1	-0.14	9.40	10.53	10.07
S0.6&D5	30.2	130.7	-0.06	8.63	10.76	9.94
S0.8&D1	40.3	61.2	-0.27	12.31	11.78	12.42
S0.8&D2	40.3	69.4	-0.22	10.74	12.17	12.18
S0.8&D3	40.3	87.1	-0.05	8.82	11.18	10.54
S0.8&D4	40.3	89.9	0.06	7.06	9.47	9.26
S0.8&D5	40.3	105.8	0.04	6.75	9.32	8.99

other tensile crack grow from the outer tip of F1 and approximately propagate in the direction of maximum principal stress to the top and bottom boundary, respectively. Meanwhile, two shear cracks initiate from the outer tip of F2 and propagate to the boundaries of rock specimens in the upward and downward directions (Figure 9(c)). With further loading, the generated cracks become longer and wider along the previous track with increasing load (Figure 9(d)). When the fissured rock is loaded at 200 μs, a secondary shear crack is generated from and propagates downward in the load direction. The propagation and coalescence of these cracks eventually form the mixed tensile-shear failure mode through the entire specimen (Figure 9(f)).

Figure 10 shows the progressive failure process of No. S0.8&D6 fissured specimen, which prominently feature pure shear failure. When the fissured rock is loaded at 142 μs (Figure 10(b)), two cracks initiate from the inner tips of the preexisting fissures, coalesce with each other, and form the shear crack in the rock bridge area. At 155 μs, two shear cracks emerge from the outer tips of F2 and further propagate to the boundaries of fissured rocks. Meanwhile, the other shear cracks initiate from the outer tips of F1 and propagate upward and downward along the principal stress direction to the boundaries of the specimen. Then, the propagation of existing cracks forms a pair of conjugate shear belts, and the secondary shear crack emerges. Eventually, the unparallel-fissured rock specimen S0.8&D6 features a pure shear failure at the end of loading due to the interaction of these shear cracks. The crack trajectory shows a nonlinear propagation, which may be induced via the presence of large sand grains in rocks.

3.3. Fragmentation and Size Distribution.

Since the fragment distribution of unparallel-fissured rock specimen under coupled static-dynamic loading is a momentous and fundamental index to assess the breakage of underground rocks subjected to the blasting or drilling, the sieving tests were conducted on the final fragmented specimens using the circular vibrating screen with the mesh sizes of 0.075, 0.25, 0.5, 1, 2, 5, 10, 20, and 40 mm. Figure 11 gives an indication of the fragment size distribution of the unparallel-fissured specimens under different static prestresses. Under a fixed static prestress, the cumulative mass fraction of fragmented specimens show that the rock specimen is more fragmented under higher loading rate. The initiation and propagation of fractures in the rocks are obviously promoted by the increasing dynamic loading rate, resulting in more pulverized fragments.

To quantitatively describe the statistical characteristics of rock fragmentation, a three-parameter generalized extreme value (GEV) distribution function was introduced [55, 56]:

$$F(d\,;\xi,\eta,\lambda) = \exp\left\{-\left[1 + \xi\left(\frac{d-\mu}{\lambda}\right)\right]^{-1/\xi}\right\}, \quad (6)$$

where d is the fragment size; the shape parameter (ξ) reflects the kurtosis and skewness of distribution curve; the location parameter (μ) represents the averaged fragment size of the broken specimen, characterizing the concentrated tendency of the fragment size; the scale parameter (λ) stands for the distribution range of fragment size. Hence, a further investigation of the variation tendency of μ and λ can give an intensive description on the effects of loading rate and static
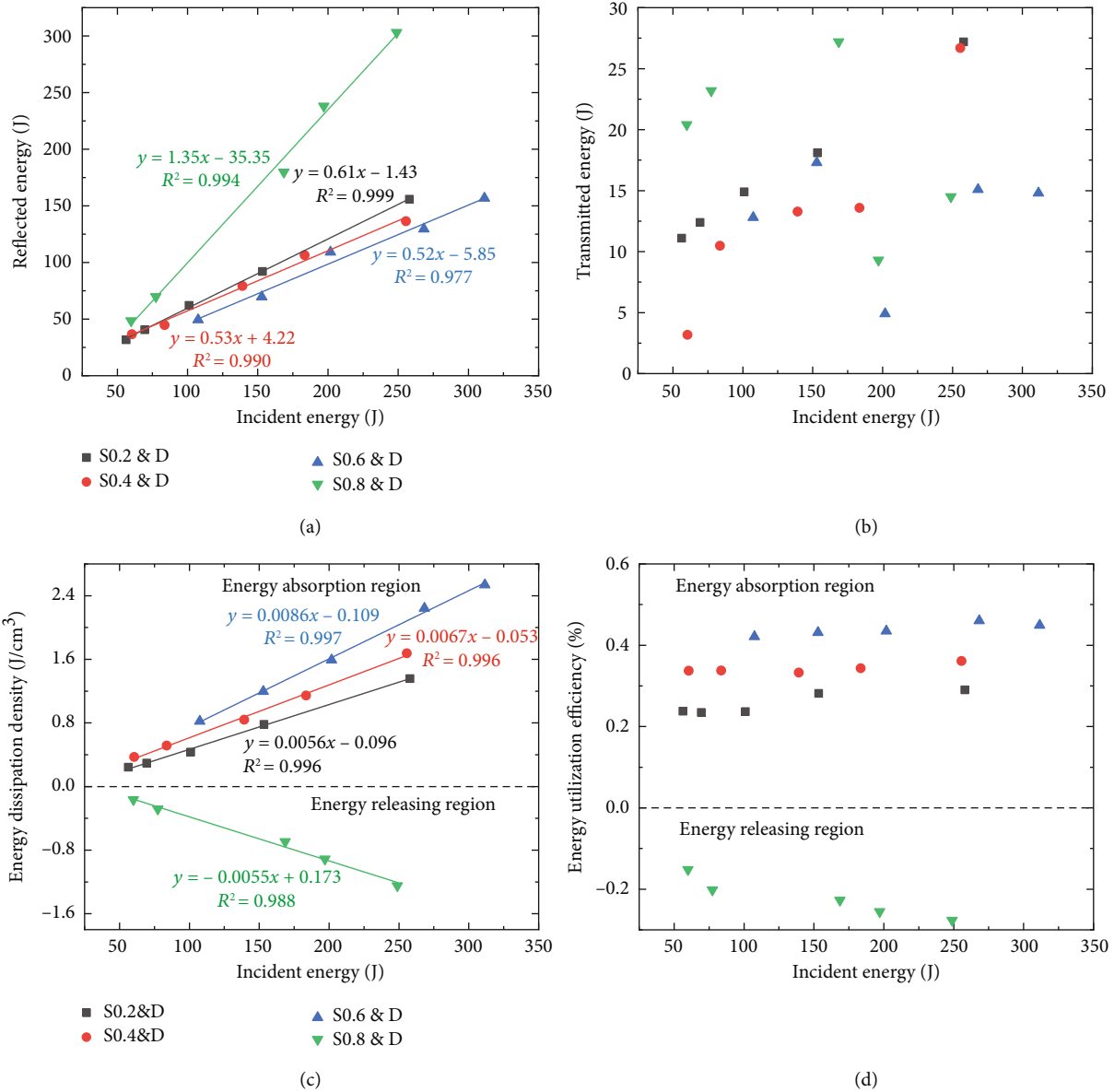
(a)

(b)

(c)

(d)

FIGURE 13: Relationships between the incident energy and (a) the reflected energy, (b) the transmitted energy, (c) energy dissipation density, and (d) the energy utilization efficiency of the unparallel-flawed sandstones.

prestress on the rock fragmentation. Figure 12 demonstrates the location parameter μ and the scale parameter λ of the fragment size distribution of the unparallel-fissured specimens under different coupled static-dynamic loads, and details are shown in Table 3. For a given static prestress, as the loading rate increases, μ linearly decreases, and λ also decreases except for that under $0.2\sigma_s$ and loading rate of $48.3\,\mathrm{s}^{-1}$, indicating that averaged fragment size and distribution range of the broken specimen decrease with increasing loading rate. This further confirms that the unparallel-fissured rocks are more fragmented for a higher dynamic loading rate. For an almost constant loading rate, the scale parameter λ exhibits irregular varying trend as the static prestress increases, while the location parameter μ shows an obvious decreasing trend. This indicates that the higher

static prestress on the unparallel-fissured rocks results in the more fracturing specimen under dynamic disturbance.

3.4. Energy Characteristics. Figure 13 depicts the relationships between the incident energy and the reflected energy, transmitted energy, energy dissipation density, and energy utilization efficiency of the unparallel-fissured sandstones; the details are listed in Table 4.

The transmitted energy of fissured sandstone shows an irregular distribution with increasing incident energy, as shown in Figure 13(b). Both reflected energy and energy dissipation density exhibit an obvious linear increase with increasing incident energy, as shown in Figures 13(a) and 13(c). The incident energy-reflected energy curve of the fissured specimens under static prestress has a significantly

TABLE 4: Energy partitions of unparallel-fissured specimens under different coupled static-dynamic loads.

Notation	Incident energy (J)	Reflected energy (J)	Transmitted energy (J)	Dissipated energy (J)	Energy dissipation density (J/cm^3)	Energy utilization efficiency (%)
S0.2&D1	56.3	31.8	11.1	13.4	0.24	0.24
S0.2&D2	69.4	40.7	12.4	16.3	0.30	0.23
S0.2&D3	101.0	62.2	14.9	23.9	0.43	0.24
S0.2&D4	153.4	92.1	18.1	43.2	0.78	0.28
S0.2&D5	257.9	155.8	27.2	74.9	1.36	0.29
S0.4&D1	60.4	36.8	3.2	20.4	0.37	0.34
S0.4&D2	83.7	44.9	10.5	28.3	0.51	0.34
S0.4&D3	139.1	79.5	13.3	46.3	0.84	0.33
S0.4&D4	183.4	106.7	13.6	63.1	1.14	0.34
S0.4&D5	255.6	136.5	26.7	92.4	1.68	0.36
S0.6&D1	107.5	49.4	12.8	45.3	0.82	0.42
S0.6&D2	152.9	69.6	17.3	66	1.20	0.43
S0.6&D3	201.8	109.1	4.9	87.8	1.59	0.44
S0.6&D4	268.3	129.6	15.1	123.6	2.24	0.46
S0.6&D5	311.5	156.8	14.8	139.9	2.54	0.45
S0.8&D1	59.9	48.6	20.4	-9.1	-0.17	-0.15
S0.8&D2	77.4	69.8	23.2	-15.6	-0.28	-0.20
S0.8&D3	168.6	179.7	27.2	-38.3	-0.69	-0.23
S0.8&D4	197.1	238.1	9.3	-50.3	-0.91	-0.26
S0.8&D5	248.9	303.2	14.5	-68.8	-1.25	-0.28

larger slope than that of the other counterparts. The energy utilization efficiency of the fissured rock specimen is 0.23-0.46 with a static prestress below 60% UCS and increases with increasing static prestress for a given incident energy. However, under identical static prestress, the energy utilization efficiency shows small changes with increasing incident energy. Under the static prestress below 80% UCS, the absolute value of the energy utilization efficiency depends on the loading rate.

Under a low dynamic strain rate, small cracks initiate and extend in fissured specimens accompanied by less energy dissipation. With increasing dynamic strain rate, fissured rocks can absorb more energy in a short time to form more shear cracks. During the dynamic loading process, rock specimens must generally absorb sufficient energy from exterior impacts for crack generation and propagation during the loading process; and the incident energy is generally greater than the reflected energy. Under coupled static and dynamic states, the main energy in the loading system dissipates for crack propagation, and the remaining small parts are utilized for rock splashing. When the applied static prestress is less than 0.8 σ_s, the existing static preload compresses the preexisting microstructures, which induce more energy dissipation within the fissured specimen. Thus, a higher static prestress can induce greater energy dissipation density and energy utilization efficiency when the static prestress is less than 0.8 σ_s. However, the reflected energy is larger than the incident energy of fissured sandstone under the static prestress of 0.8 σ_s, and the corresponding dissipated energy is negative. This phenomenon may be induced by the release of elastic energy stored within the rock mate-

rial generated by the static precompression, and the remaining part of the elastic energy is transmitted to the transmitted bar. In addition, the static prestress has no significant regular effect on the energy evolution of fissured specimens.

4. Discussion

When the fissured rocks are subjected to exterior disturbance, new cracks generally generate along the preexisting discontinuities and propagate within rock materials, leading to ultimate failures with different patterns. In practice, the evolution of generated cracks accompanied by energy dissipation significantly affects the failure mode and mechanical response of fissured rocks. Therefore, there is a correlation among the energy dissipation, mechanical responses, and broken fragments, as shown in Figure 14. When the static prestress is less than 0.8 σ_s, the energy dissipation density and coupled strength are positively correlated with each other. However, the location parameter μ exhibits negative correlations with the energy dissipation density and coupled strength. For a static prestress below 0.8 σ_s, the higher dynamic strain rate of fissured rocks indicates that the greater energy dissipates in an extremely short time. Thus, more preexisting microdiscontinuities in rock materials are activated to form more macrocracks to absorb the exterior energy and more fragments with smaller sizes. In addition, the higher dynamic strain rate can induce the deformation hysteresis of fissured sandstone during the loading process, which contributes to the strengthening effect of the coupled strength of the fissured specimen. Thus, a greater dynamic
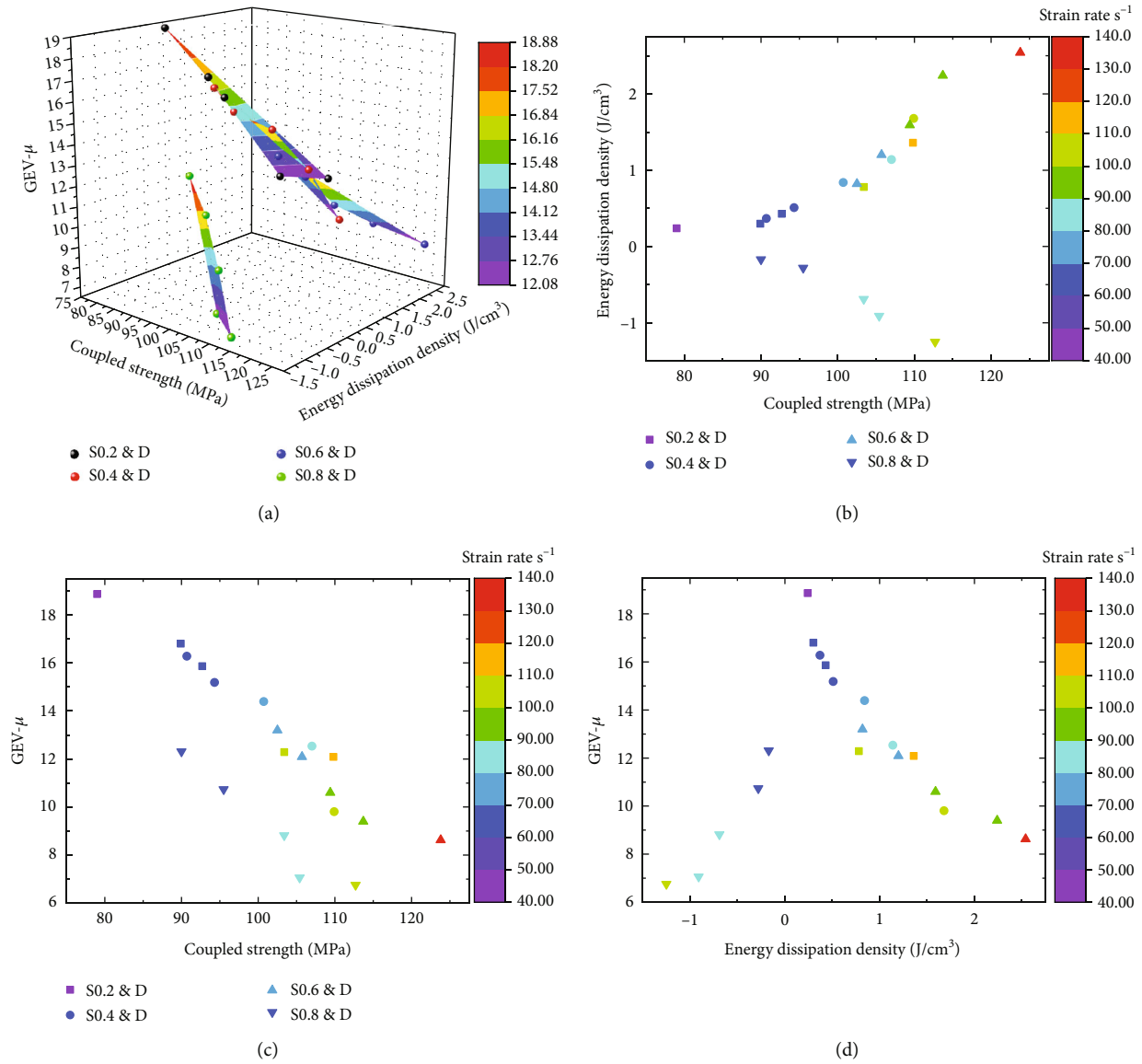
FIGURE 14: Relationships between the coupled strength, fragment dimension, and energy dissipation density of the unparallel-flawed rock specimens: (a) 3D view of relationship of location parameter μ–coupled strength–energy dissipation density; (b) coupled strength vs. fractal dimension; (c) coupled strength vs. GEV-μ; (d) energy dissipation density vs. GEV-μ.

coupled strength corresponds to a greater energy dissipation density with increasing dynamic strain rate. In other words, when the dissipated energy increases, the fragments become finer, and the mechanical response strengthens. This corresponding result may contribute to estimating the fragment size distribution in many rock engineering applications, such as rockfalls, mineral processing, or blasting.

When the static prestress is 0.8 σ_s, the energy dissipation density and location parameter μ show a positive correlation with each other. However, the coupled strength shows negative correlations with the energy dissipation density and location parameter μ. Since the released elastic energy is stored in the rock material generated by the static precompression, the energy dissipation density is negative under the static prestress of 0.8 σ_s, which corresponds to energy

release. When the static prestress is 0.8 σ_s, more damage emerges within the rock material, which generates more crack and wreak the coupled strength of the specimen. In other words, when less energy is released within the rock specimen, the coupled strength is higher, and the specimens are more fragmented.

5. Conclusions

Rocks containing preexisting discontinuities are likely simultaneously subjected to static precompression and dynamic disturbance. However, the mechanical behaviors and fracturing mechanism of fissured rocks under coupled static-dynamic loads remain far from being fully understood. In this study, a series of SHPB laboratory experiments

were performed to systematically investigate the coupled static-dynamic strength, failure behaviors, fragmentation, and energy characteristics of unparallel fissured sandstones subjected to coupled static-dynamic loads.

A strain-rate dependence of the mechanical response, fragment size, and energy characteristics of prestressed rocks is observed based on the increasing coupled dynamic strength, decreasing location parameter μ, and increasing energy dissipation density with increasing dynamic strain rate. The failure modes of fissured sandstone highly depend on the dynamic strain rate. The ultimate failure pattern gradually changes from the tensile failure mode to the mixed tensile-shear failure mode and subsequently to the shear failure mode with increasing strain rate. The fragmentation of unparallel-fissured rocks is promoted by the static prestress under dynamic disturbance. Under a given dynamic strain rate, the highest coupled dynamic strength occurs in the fissured sandstone with a static prestress of 0.6 σ_s due to the compressive effect on preexisting microstructures in the rock material. A higher static prestress can induce greater energy dissipation density and energy utilization efficiency when the static prestress is less than 0.8 σ_s, which is consistent with the evolution of the coupled strength with increasing static prestress. When the static prestress reaches 0.8 σ_s, the released elastic energy by the precompressed rocks is greater than the incident energy, and the corresponding dissipated energy is negative.

Data Availability

Data and material used in preparation of this manuscript are available from the corresponding authors upon reasonable request if not already in the public domain.

Conflicts of Interest

All authors declare that they have no known competing financial interests or personal relationships that could have appeared to influence the work reported in this paper.

Acknowledgments

References

[1] G. Gao, M. A. Meguid, and L. E. Chouinard, "On the role of pre-existing discontinuities on the micromechanical behavior of confined rock samples: a numerical study," *Acta Geotechnica*, vol. 15, no. 12, pp. 3483–3510, 2020.

[2] S. F. Wang, Y. Jing, Z. Z. Pi, S. Y. Wang, and Z. L. Zhou, "Strength and failure properties of preflawed granite under coupled biaxial loading and unloading conditions," *Lithosphere*, vol. 2021, no. Special 7, article 9320619, 2022.

[3] H. B. Du, F. Dai, Y. Liu, Y. Xu, and M. D. Wei, "Dynamic response and failure mechanism of hydrostatically pressurized rocks subjected to high loading rate impacting," *Soil Dynamics and Earthquake Engineering*, vol. 129, article 105927, 2020.

[4] X. Cai, Z. Zhou, and X. Du, "Water-induced variations in dynamic behavior and failure characteristics of sandstone subjected to simulated geo-stress," *International Journal of Rock Mechanics and Mining Sciences*, vol. 130, article 104339, 2020.

[5] H. B. Du, F. Dai, M. D. Wei, A. Li, and Z. L. Yan, "Dynamic compression–shear response and failure criterion of rocks with hydrostatic confining pressure: an experimental investigation," *Rock Mechanics and Rock Engineering*, vol. 54, no. 2, pp. 955–971, 2021.

[6] A. Li, F. Dai, Y. Liu, H. B. Du, and R. Jiang, "Dynamic stability evaluation of underground cavern sidewalls against flexural toppling considering excavation-induced damage," *Tunnelling and Underground Space Technology*, vol. 112, article 103903, 2021.

[7] M. A. Brideau, M. Yan, and D. Stead, "The role of tectonic damage and brittle rock fracture in the development of large rock slope failures," *Geomorphology*, vol. 103, no. 1, pp. 30–49, 2009.

[8] H. B. Du, F. Dai, Y. Xu, Y. Liu, and H. N. Xu, "Numerical investigation on the dynamic strength and failure behavior of rocks under hydrostatic confinement in SHPB testing," *International Journal of Rock Mechanics and Mining Sciences*, vol. 108, pp. 43–57, 2018.

[9] P. Feng, Y. Xu, and F. Dai, "Effects of dynamic strain rate on the energy dissipation and fragment characteristics of cross-fissured rocks," *International Journal of Rock Mechanics and Mining Sciences*, vol. 138, article 104600, 2021.

[10] P. Tang, X. Ma, Y. Zhao et al., "Experimental research on the effect of bedding angle on the static and dynamic behaviors of burst-prone sandstone," *Lithosphere*, vol. 2022, no. Special 11, article 6933410, 2022.

[11] P. Feng, B. Liu, R. Tang, M. D. Wei, Y. Zhang, and H. Li, "Dynamic fracture behaviors and fragment characteristics of pre-compressed flawed sandstones," *International Journal of Mechanical Sciences*, vol. 220, article 107162, 2022.

[12] X. B. Li, F. Q. Gong, M. Tao et al., "Failure mechanism and coupled static-dynamic loading theory in deep hard rock mining: a review," *Journal of Rock Mechanics and Geotechnical Engineering*, vol. 9, no. 4, pp. 767–782, 2017.

[13] Y. Xu, F. Dai, and H. B. Du, "Experimental and numerical studies on compression-shear behaviors of brittle rocks subjected to combined static-dynamic loading," *International Journal of Mechanical Sciences*, vol. 175, article 105520, 2020.

[14] P. Feng, F. Dai, Y. Liu, and H. B. Du, "Mechanical behaviors of rock-like specimens with two non-coplanar fissures subjected to coupled static-dynamic loads," *Engineering Fracture Mechanics*, vol. 199, pp. 692–704, 2018.

[15] P. Feng, J. C. Zhao, F. Dai, M. D. Wei, and B. Liu, "Mechanical behaviors of conjugate-flawed rocks subjected to coupled static–dynamic compression," *Acta Geotechnica*, vol. 17, no. 5, pp. 1765–1784, 2022.

[16] Y. Yang, J. M. Chen, and T. H. Huang, "Effect of joint sets on the strength and deformation of rock mass models," *International Journal of Rock Mechanics and Mining Sciences*, vol. 35, no. 1, pp. 75–84, 1998.

[17] J. Liu, E. Y. Wang, D. Z. Song, S. H. Wang, and Y. Niu, "Effect of rock strength on failure mode and mechanical behavior of composite samples," *Arabian Journal of Geosciences*, vol. 8, no. 7, pp. 4527–4539, 2015.

[18] F. Luo, G. Li, and H. Zhang, "Mechanical behavior and damage mechanism of loaded coal and rock," *World Journal of Engineering*, vol. 14, no. 3, pp. 200–207, 2017.

[19] A. Bobet and H. H. Einstein, "Fracture coalescence in rock-type materials under uniaxial and biaxial compression," *International Journal of Rock Mechanics and Mining Sciences*, vol. 35, no. 7, pp. 863–888, 1998.

[20] Y. P. Li, L. Z. Chen, and Y. H. Wang, "Experimental research on pre-cracked marble under compression," *International Journal of Solids and Structures*, vol. 42, no. 9-10, pp. 2505–2516, 2005.

[21] H. Q. Li and L. N. Y. Wong, "Influence of flaw inclination angle and loading condition on crack initiation and propagation," *International Journal of Solids and Structures*, vol. 49, no. 18, pp. 2482–2499, 2012.

[22] Y. L. Zhao, L. Y. Zhang, W. J. Wang, C. Z. Pu, W. Wan, and J. Z. Tang, "Cracking and stress–strain behavior of rock-like material containing two flaws under uniaxial compression," *Rock Mechanics and Rock Engineering*, vol. 49, no. 7, pp. 2665–2687, 2016.

[23] S. Q. Yang and Y. H. Huang, "An experimental study on deformation and failure mechanical behavior of granite containing a single fissure under different confining pressures," *Environmental Earth Sciences*, vol. 76, no. 10, pp. 1–22, 2017.

[24] H. L. Le, S. R. Sun, P. H. Kulatilake, and J. H. Wei, "Effect of grout on mechanical properties and cracking behavior of rock-like specimens containing a single flaw under uniaxial compression," *International Journal of Geomechanics*, vol. 18, no. 10, article 04018129, 2018.

[25] L. E. Vallejo, "Fissure parameters in stiff clays under compression," *Journal of Geotechnical Engineering*, vol. 115, no. 9, pp. 1303–1317, 1989.

[26] H. Cheng, X. P. Zhou, J. Zhu, and Q. H. Qian, "The effects of crack openings on crack initiation, propagation and coalescence behavior in rock-like materials under uniaxial compression," *Rock Mechanics and Rock Engineering*, vol. 49, no. 9, pp. 3481–3494, 2016.

[27] L. N. Y. Wong and H. H. Einstein, "Crack coalescence in molded gypsum and Carrara marble: part1. Macroscopic observations and interpretation," *Rock Mechanics and Rock Engineering*, vol. 42, no. 3, pp. 475–511, 2009.

[28] S. P. Morgan and H. H. Einstein, "Cracking processes affected by bedding planes in Opalinus shale with flaw pairs," *Engineering Fracture Mechanics*, vol. 176, pp. 213–234, 2017.

[29] R. H. Wong and K. T. Chau, "Crack coalescence in a rock-like material containing two cracks," *International Journal of Rock Mechanics and Mining Sciences*, vol. 35, no. 2, pp. 147–164, 1998.

[30] M. Sagong and A. Bobet, "Coalescence of multiple flaws in a rock-model material in uniaxial compression," *International Journal of Rock Mechanics and Mining Sciences*, vol. 39, no. 2, pp. 229–241, 2002.

[31] C. Zou and L. N. Y. Wong, "Experimental studies on cracking processes and failure in marble under dynamic loading," *Engineering Geology*, vol. 173, pp. 19–31, 2014.

[32] C. J. Zou, L. N. Y. Wong, and Y. Cheng, "The Strength and Crack Behavior of the Rock-like Gypsum under High Strain Rate," in *46th US Rock Mechanics/Geomechanics Symposium*, Chicago, Illinois, 2012.

[33] C. J. Zou, L. N. Y. Wong, J. J. Loo, and B. S. Gan, "Different mechanical and cracking behaviors of single-flawed brittle gypsum specimens under dynamic and quasi-static loadings," *Engineering Geology*, vol. 201, pp. 71–84, 2016.

[34] X. B. Li, T. Zhou, and D. Y. Li, "Dynamic strength and fracturing behavior of single-flawed prismatic marble specimens under impact loading with a split-Hopkinson pressure bar," *Rock Mechanics and Rock Engineering*, vol. 50, no. 1, pp. 29–44, 2017.

[35] D. Y. Li, Z. Y. Han, X. L. Sun, T. Zhou, and X. B. Li, "Dynamic mechanical properties and fracturing behavior of marble specimens containing single and double flaws in SHPB tests," *Rock Mechanics and Rock Engineering*, vol. 52, no. 6, pp. 1623–1643, 2019.

[36] Z. L. Yan, F. Dai, Y. Liu, and H. B. Du, "Experimental investigations of the dynamic mechanical properties and fracturing behavior of cracked rocks under dynamic loading," *Bulletin of Engineering Geology and the Environment*, vol. 79, no. 10, pp. 5535–5552, 2020.

[37] P. Feng, F. Dai, Y. Liu, N. W. Xu, and T. Zhao, "Influence of two unparallel fissures on the mechanical behaviours of rock-like specimens subjected to uniaxial compression," *European Journal of Environmental and Civil Engineering*, vol. 24, no. 10, pp. 1643–1663, 2020.

[38] H. Lee and S. Jeon, "An experimental and numerical study of fracture coalescence in pre-cracked specimens under uniaxial compression," *International Journal of Solids and Structures*, vol. 48, no. 6, pp. 979–999, 2011.

[39] L. O. Afolagboye, J. He, and S. J. Wang, "Experimental study on cracking behaviour of moulded gypsum containing two non-parallel overlapping flaws under uniaxial compression," *Acta Mechanica Sinica*, vol. 33, no. 2, pp. 394–405, 2017.

[40] S. Q. Yang, X. R. Liu, and H. W. Jing, "Experimental investigation on fracture coalescence behavior of red sandstone containing two unparallel fissures under uniaxial compression," *International Journal of Rock Mechanics and Mining Sciences*, vol. 63, pp. 82–92, 2013.

[41] Y. H. Huang, S. Q. Yang, and W. Zeng, "Experimental and numerical study on loading rate effects of rock-like material specimens containing two unparallel fissures," *Journal of Central South University*, vol. 23, no. 6, pp. 1474–1485, 2016.

[42] Y. X. Zhou, K. W. Xia, X. B. Li et al., "Suggested methods for determining the dynamic strength parameters and mode-I fracture toughness of rock materials," *International Journal of Rock Mechanics and Mining Sciences*, vol. 49, pp. 105–112, 2012.

[43] X. Cai, Z. Zhou, H. Zang, and Z. Song, "Water saturation effects on dynamic behavior and microstructure damage of sandstone: phenomena and mechanisms," *Engineering Geology*, vol. 276, article 105760, 2020.

[44] X. Cai, C. Cheng, Y. Zhao, Z. Zhou, and S. Wang, "The role of water content in rate dependence of tensile strength of a fine-grained sandstone," *Engineering*, vol. 22, no. 1, article 58, 2022.

[45] H. B. Du, F. Dai, Y. Xu, Z. Yan, and M. D. Wei, "Mechanical responses and failure mechanism of hydrostatically pressurized rocks under combined compression-shear impacting," *International Journal of Mechanical Sciences*, vol. 165, article 105219, 2020.

[46] J. Blaber, B. Adair, and A. Antoniou, "Ncorr: open-source 2D digital image correlation matlab software," *Experimental Mechanics*, vol. 55, no. 6, pp. 1105–1122, 2015.

[47] A. Weidner and H. Biermann, "Review on strain localization phenomena studied by high-resolution digital image correlation," *Advanced Engineering Materials*, vol. 23, no. 4, article 2001409, 2021.

[48] Y. Q. Bao, D. Y. Feng, N. Ma, H. H. Zhu, and T. Rabczuk, "Experimental and numerical study on structural performance of reinforced concrete box sewer with localized extreme defect," *Underground Space*, vol. 3, no. 2, pp. 166–179, 2018.

[49] W. G. Zhang, X. Gu, W. H. Zhong, Z. T. Ma, and X. M. Ding, "Review of transparent soil model testing technique for underground construction: ground visualization and result digitalization," *Underground Space*, vol. 7, no. 4, pp. 702–723, 2022.

[50] M. Chen, S. Q. Yang, R. P. Gamage et al., "Fracture processes of rock-like specimens containing nonpersistent fissures under uniaxial compression," *Energies*, vol. 12, no. 1, p. 79, 2019.

[51] D. Y. Li, P. Xiao, Z. Y. Han, and Q. Q. Zhu, "Mechanical and failure properties of rocks with a cavity under coupled static and dynamic loads," *Engineering Fracture Mechanics*, vol. 225, article 106195, 2020.

[52] Z. L. Zhou, X. Cai, X. B. Li, W. Z. Cao, and X. M. Du, "Dynamic response and energy evolution of sandstone under coupled static–dynamic compression: insights from experimental study into deep rock engineering applications," *Rock Mechanics and Rock Engineering*, vol. 53, no. 3, pp. 1305–1331, 2020.

[53] M. Hokka, J. Black, D. Tkalich et al., "Effects of strain rate and confining pressure on the compressive behavior of Kuru granite," *International Journal of Impact Engineering*, vol. 91, pp. 183–193, 2016.

[54] Z. L. Yan, F. Dai, J. B. Zhu, and Y. Xu, "Dynamic cracking behaviors and energy evolution of multi-flawed rocks under static pre-compression," *Rock Mechanics and Rock Engineering*, vol. 54, no. 9, pp. 5117–5139, 2021.

[55] J. D. Hogan, R. J. Rogers, J. G. Spray, and S. Boonsue, "Dynamic fragmentation of granite for impact energies of 6-28 J," *Engineering Fracture Mechanics*, vol. 79, pp. 103–125, 2012.

[56] W. G. Shen, G. Luo, and X. Y. Zhao, "On the impact of dry granular flow against a rigid barrier with basal clearance via discrete element method," *Landslides*, vol. 19, no. 2, pp. 479–489, 2022.